ChemComm

# Natural abundance solid-state $^{33}S$ NMR study of $NbS_3$: applications for battery conversion electrodes



| | |
|---|---|
| Journal: | *ChemComm* |
| Manuscript ID | CC-COM-08-2019-006059.R1 |
| Article Type: | Communication |
| | |

Journal Name

COMMUNICATION

# Natural abundance solid-state $^{33}$S NMR study of $NbS_3$: applications for battery conversion electrodes

Received 00th January 20xx,
Accepted 00th January 20xx

DOI: 10.1039/x0xx00000x

www.rsc.org/

David M. Halat,[a,†] Sylvia Britto,[a,‡] Kent J. Griffith,[a,] Erlendur Jónsson,[a,b] and Clare P. Grey[a,*]

**We report ultra-wideline, high-field natural abundance solid-state $^{33}$S NMR spectra of the Li-ion battery conversion electrode $NbS_3$, the first $^{33}$S NMR study of a compound containing disulfide ($S_2^{2-}$) units. The large quadrupolar coupling parameters ($C_Q$ ≈ 31 MHz) are consistent with values obtained from DFT calculations, and the spectra provide evidence for the linear Peierls distortion that doubles the number of $^{33}$S sites.**

Transition metal sulfides with disulfide linkages, such as vanadium sulfide ($VS_4$) and niobium sulfide ($NbS_3$), the subject of this paper, have technological importance as potential electrode materials for lithium-ion batteries.[1–4] Redox activity in most battery materials is centred on the transition metal (TM), and only recently has (oxygen) anionic redox been identified as the source of the high capacities (>300 mAh g$^{-1}$) exhibited by some lithium-excess oxides.[5] The electrochemical conversion mechanisms of electrode materials based on TM sulfides with disulfide ($S_2^{2-}$) linkages are also attributed to anionic redox activity, which comprises reduction of $S_2^{2-}$ to $S^{2-}$ during discharge, giving rise to high capacities (~1000 mAh g$^{-1}$) and eventually forming $Li_2S$ and the reduced metal.[1,6,7] $NbS_3$ contains both $S^{2-}$ and $S_2^{2-}$, and thus the corresponding (de)lithiation processes are expected to be even more complex. Indeed, in many such systems the precise redox mechanisms remain poorly understood, with direct evidence of $S_2^{2-}$ coming primarily from Raman spectroscopy.[8]

Whereas many prior studies on Li-ion battery materials have employed $^{6/7}$Li solid-state NMR experiments,[9,10] very few solid-state $^{33}$S NMR studies of any kind have been reported, due to the low gyromagnetic ratio ($1/13$ that of $^1$H), very low natural abundance (0.76%), and large quadrupolar moment ($I$ = 3/2) of $^{33}$S.[11–15] Recent $^{33}$S NMR studies of Li-S and Mg-S battery systems have identified the discharge products ($Li_2S$ and MgS),[16,17] which contain $S^{2-}$ in tetrahedral environments, but the technique has not been applied to study sulfide-based conversion electrodes. Previous $^{33}$S NMR studies on functional inorganic sulfides include TM disulfides (*e.g.,* $MoS_2$ and $TiS_2$), where trigonal pyramidal $S^{2-}$ environments give rise to large quadrupolar coupling constants ($C_Q$) of 2–10 MHz and correspondingly broad NMR powder patterns *via* second-order quadrupolar (SOQ) broadening of the $I$ = 3/2 central transition.[11] Thus far, $^{33}$S NMR has not been reported in sulfides containing disulfide groups, which should prove more challenging due to the highly asymmetric and covalent environment of S in $S_2^{2-}$. (To our knowledge, the largest reported $^{33}$S $C_Q$ is ~43 MHz, for an isotopically enriched sample of elemental sulfur.[18])

Because of the inherent insensitivity and strongly quadrupolar nature of $^{33}$S, signal-enhancing NMR methods are typically employed, such as (1) high magnetic field strengths to minimise SOQ broadening[19,20] and (2) specialised pulse sequences including Quadrupolar Carr-Purcell-Meiboom-Gill (QCPMG) experiments and/or population transfer experiments such as double-frequency sweeps (DFS).[21–23] Magic-angle spinning (MAS), while effective in highly symmetrical systems (*e.g.* sulfates), only partially averages the SOQ interaction and is not commonly used when the $^{33}$S $C_Q$ exceeds 2 MHz.[11,24]

In this work, we show that ultra-wideline, natural abundance $^{33}$S static spectra of $NbS_3$ can be readily acquired at high field (20 T) in a reasonable time frame (~6 h) using the DFS-QCPMG pulse sequence. Spectral features corresponding to both $S^{2-}$ and $S_2^{2-}$ environments in $NbS_3$ can be distinguished and the corresponding quadrupolar parameters extracted; the $C_Q$ values are shown to be consistent with, though slightly larger than, those obtained from first-principles density functional theory (DFT) calculations. The DFT calculations also reveal clear differences in the calculated quadrupolar asymmetry parameters ($\eta_Q$) of $S_2^{2-}$ sites, due to the linear Peierls distortion (alternation of short and long Nb–Nb distances) in

[a] *Department of Chemistry, University of Cambridge, Lensfield Road, Cambridge CB2 1EW, U.K.*
[b] *Department of Physics, Chalmers University of Technology, 412 96 Gothenburg, Sweden*
Current addresses: †*Dept. of Chemical and Biomolecular Engineering, University of California, Berkeley, CA 94720, U.S.*; ‡*Diamond Light Source Ltd., Harwell Science and Innovation Campus, Didcot, OX11 0DE, U.K.*; *Dept. of Materials Science and Engineering, Northwestern University, Evanston, IL 60208, U.S.*
* To whom correspondence should be addressed
Electronic Supplementary Information (ESI) available: synthesis and XRD patterns; DFT calculation details; analysis of $^{33}$S NMR spectra. See DOI: 10.1039/x0xx00000x

$NbS_3$ chains, which we rationalise as a function of the local S bonding environments. Moreover, the experimental $^{33}$S NMR spectra show evidence of the expected doubling of disulfide sites as a consequence of this distortion. Finally, we show that $^{33}$S spectral signatures (*i.e.* SOQ discontinuities) corresponding to $S_2^{2-}$ can be acquired in as little as 20 minutes, which should in future enable rapid elucidation of anionic redox mechanisms in cycled electrodes.

The pseudo one-dimensional triclinic structure of $NbS_3$ (space group $P\bar{1}$) comprises trigonal prismatic [$NbS_6$] units connected into $NbS_3$ chains extending along the *b*-axis (Figure 1); these chains are arranged into sheets (along *a*) which are stacked along *c*, and held together through weak van der Waals forces.[25,26] The molecular formula can be written $Nb^{4+}(S_2^{2-})S^{2-}$, *i.e.*, sulfur is present as both sulfide ($S^{2-}$) ions and disulfide ($S_2^{2-}$) groups. Chain polytypism can result from variations in the stacking arrangements of chains and/or sheets.[27,28] Powder XRD patterns of our $NbS_3$ samples (Figure SI1) show absent (*h*0*l*) reflections, which suggest disorder in the stacking sequences of $NbS_3$ sheets along *c*.[28,29] Importantly for the NMR experiments, the local S environments are unaffected by stacking faults as the registry between $NbS_3$ sheets is independent of the stacking configuration (further details provided in Figure SI2 and the SI).

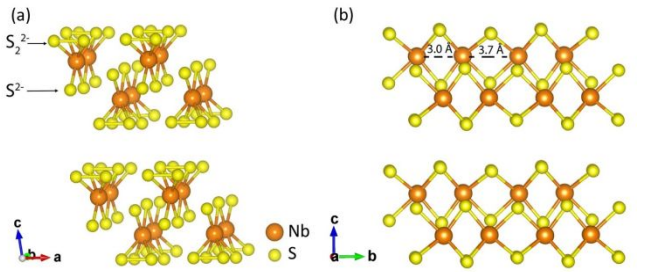


Figure 1: Structure of $NbS_3$ (space group $P\bar{1}$) as reported by Rijnsdorp and Jellinek,[25] viewed (a) down the *b* direction and (b) down the *a* direction. The structure consists of trigonal prismatic chains along the *b* axis, which stack along the *a* axis into sheets; the sheets stack along *c*. In (b), the Peierls distortion is evident from the alternating short (3.0 Å) and long (3.7 Å) Nb–Nb distances within the chains along the *b* direction.

As seen in related early-TM oxides and sulfides such as $VO_2$ and $VS_4$,[30–32] the $NbS_3$ chains undergo a linear Peierls distortion wherein adjacent Nb sites pair to give alternating short (3.0 Å) and long (3.7 Å) Nb–Nb distances.[33] As a consequence, $NbS_3$ exhibits (1) diamagnetic behaviour in a nominally $d^1$ ($Nb^{4+}$) system and (2) doubling of both the unit cell along *b* as well as the number of crystallographically-distinct local environments.

To determine the feasibility of acquiring highly broadened, natural abundance $^{33}$S NMR spectra of $NbS_3$, as well as to guide the experimental acquisition, we first performed periodic DFT calculations of Peierls-distorted $NbS_3$ using the plane-wave CASTEP code[34] (geometry-optimised structure shown in Figure SI3 and details given in SI). As shown in Table 1, the calculated $^{33}$S quadrupolar coupling constants ($C_Q$) are highly sensitive to the chemical identity of the S sites, with isolated sulfide ions giving $C_Q$ values of 4.4 or 6.5 MHz, and the disulfide units exhibiting extremely large $C_Q$ values of ~30 MHz. A simulated $^{33}$S spectrum at 20 T using the DFT-calculated parameters is shown in Figure 2, top (full deconvolution given in Figure SI4), showing that the $S^{2-}$ features are comparatively narrow whereas the lineshapes arising from $S_2^{2-}$ span a broad frequency range, with sharp SOQ discontinuities at 10,500 ppm and –18,500 ppm.

Table 1: DFT-calculated $^{33}$S NMR parameters of $NbS_3$, with experimental fitted values (in square brackets) for comparison where applicable. Chemical shielding parameters have been converted to shifts using the relationship developed by Pallister *et al.*[21] Chemical shift anisotropy (CSA) parameters are given in the Herzfeld–Berger convention[35] with the span Ω and skew κ also converted from the calculated shielding parameters. Electric field gradient (EFG) tensors are given in the Haeberlen convention, with $C_Q$ the quadrupolar coupling constant and $\eta_Q$ the quadrupolar asymmetry parameter. Only the magnitude of the $C_Q$ value is reported; the sign is not detected in polycrystalline NMR experiments. Full DFT-calculated parameters including Euler angles are given in Tables SI2 and SI3, with more detail in the SI on Euler angle conventions. Experimental CSA parameters for the $S_2^{2-}$ sites could not be reliably determined as they have negligible influence on the observed lineshapes; they are, therefore, not reported.

| S site | Local env. | $\delta_{iso}$ (ppm) | Ω (ppm) | κ | $\lvert C_Q \rvert$ (MHz) | $\eta_Q$ |
|---|---|---|---|---|---|---|
| **S1** | $S^{2-}$ | −20 [−25] | 727 [700] | −0.55 [−0.7] | 4.4 [4] | 0.38 [0.5] |
| **S2** | | −243 [−250] | 168 [300] | −0.65 [−0.65] | 6.5 [6.5] | 0.82 [0.9] |
| **S3** | $S_2^{2-}$ | 44 | 251 | 0.69 | 30.3 [31] | 0.04 [0.05] |
| **S4** | | 113 | 531 | 0.77 | 30.5 [31] | 0.27 [0.3] |
| **S5** | | 58 | 265 | 0.51 | 30.1 [31] | 0.05 [0.05] |
| **S6** | | 112 | 491 | 0.96 | 30.3 [31] | 0.29 [0.3] |

In acquiring ultra-wideline experimental $^{33}$S NMR spectra of $NbS_3$, we found that the simulated spectrum proved invaluable; we were able to initially acquire spectra near the SOQ discontinuities to determine their exact positions, and also chose a large QCPMG spikelet spacing, due to the relatively flat predicted lineshape far from the discontinuities.

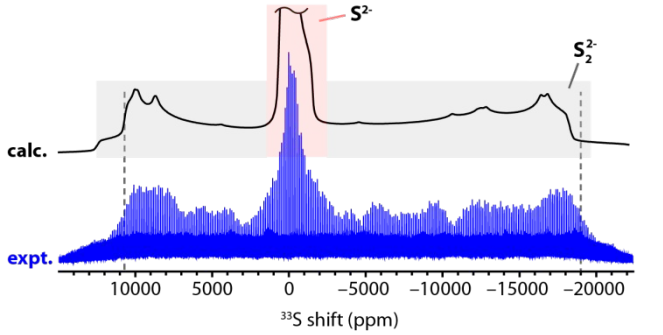


Figure 2: Simulated $^{33}$S spectrum at 20 T from DFT-calculated parameters ("calc.") and experimental ultra-wideline DFS-QCPMG static $^{33}$S spectrum of $NbS_3$ acquired at 20 T using a frequency-stepping approach ("expt."). Experimental NMR details are given in Table SI1 and the SI. Coloured boxes indicate the positions of the SOQ broadened $S^{2-}$ (pink) and $S_2^{2-}$ (grey) features; dotted lines show the discontinuities in the experimental spectrum. All simulations in this work were performed using the QUEST software of Perras et al.[36]

The broadband experimental spectrum thus obtained, presented in Figure 2 (bottom), comprises a variable-offset cumulative spectrum (VOCS)[37–39] of 17 summed sub-spectra; the experiment required 6 h in total. The spectrum is in excellent qualitative agreement with simulation, with a narrower, more intense region centred at 0 ppm

corresponding to $S^{2-}$ and a very broad feature corresponding to $S_2^{2-}$. For the latter, extremely SOQ broadened feature, the spikelet intensity falls away at roughly 10,700 ppm and –19,000 ppm (at high and low frequency, respectively), which is consistent with a $^{33}S$ site with $C_Q$ = 31 MHz, $\eta_Q$ = 0.05 centred at 0 ppm (Figure SI5), in good agreement with the calculated parameters of $S_2^{2-}$ (in particular, the S3 and S5 sites). Specifically, the edges are defined by the $\eta_Q \approx 0$ environments (S3 and S5), and the other sites (S4 and S6) contribute less obviously to the discontinuities.

Having rapidly acquired the broadband $^{33}S$ spectrum, we next collected for a longer period (~11 h) at the central $S^{2-}$ region. Figure 3a shows the experimental DFS-QCPMG spectrum of $NbS_3$ centred at 0 ppm, with the observed intensity corresponding to $S^{2-}$ sites. The initial lineshape simulated from the calculated parameters of the S1 and S2 sites shows approximate agreement with the experimental spectrum (Figure SI7). By manual adjustment of the calculated CSA and EFG parameters of the S1 and S2 sites (see SI), a simulated spectrum in better agreement with experiment was obtained (Figure 3b). The optimised parameters, which do not differ significantly from the calculated ones, are given in Table 1 (square brackets); Euler angles were not adjusted. The discrepancy in the intensity at lower frequencies is attributed to the unequal excitation of the experimental spectrum, with the carrier frequency centred at 0 ppm; further offset spectra were not acquired due to time constraints. Nonetheless, the reasonable agreement observed with only minor adjustments gives us confidence that the DFT calculations accurately capture the local $S^{2-}$ environments. The magnitude of the $C_Q$ values are also reminiscent of that of $S^{2-}$ in $TaS_2$,[11] although we note the local S symmetry is different (distorted tetrahedral in $NbS_3$ vs. trigonal in $TaS_2$).

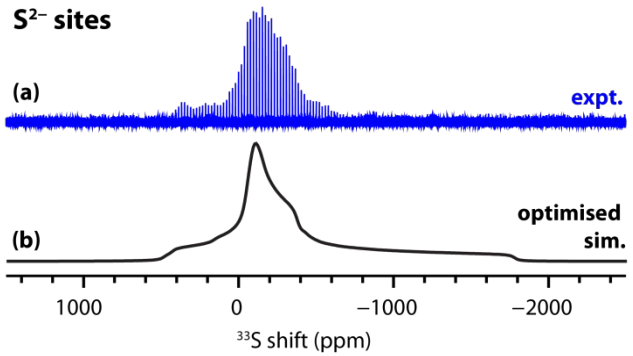


Figure 3: (a) Experimental DFS-QCPMG static $^{33}S$ spectrum of $NbS_3$ acquired at 20 T ("expt."), centred at 0 ppm to acquire resonances arising from $S^{2-}$ environments, and (b) simulated $^{33}S$ spectrum using fitted parameters of $S^{2-}$ sites ("optimised sim."). Full details are given in Tables SI1 and SI4.

We next focused our attention more closely on the high-frequency $S_2^{2-}$ SOQ discontinuity. In the simulated spectrum, this edge shows not one but two maxima (Figure 4, top), which arise from sites with differing $\eta_Q$ values. The higher-frequency maximum is associated with the S3 and S5 sites with $\eta_Q \approx 0.05$, whereas the other maximum is associated with S4 and S6 with $\eta_Q \approx 0.3$ (deconvolution shown in Figure SI4). We note that the difference in the local geometry of these sites is a consequence of the Peierls distortion; S3 and S5 bridge a short Nb–Nb pair, whereas the other $S_2^{2-}$ sites do not (Figure SI4, top left inset). As a consequence, the Nb–S(3,5)–Nb angle is ~75° whereas it is ~90° for Nb–S(4,6)–Nb due to the greater Nb–Nb distance. Given these angles, we can rationalize the different $\eta_Q$ values using the method of Autschbach *et al.*[40] The principal axis of the largest EFG tensor component $V_{zz}$ is along the covalent S–S disulfide bond (giving $\eta_Q \approx 0$); however, additional covalent bonding and coulombic interactions lift this axial symmetry and result in non-zero $\eta_Q$ values. The more favourable covalent interaction with Nb for S4 and S6 due to the 90° angle induced by the Peierls distortion leads to larger values of $\eta_Q \approx 0.3$, as confirmed by visualisation[41] of the calculated EFG tensors (Figure SI8).

A longer VOCS acquisition (~30 h) at the high-frequency edge was performed to identify this splitting of sites, a spectral signature of the Peierls distortion. The summed spectrum (Figure 4, bottom) shows evidence of the expected doubling of the features, with the positions of the maxima in reasonable agreement with the simulated spectra, recalling that the calculated $C_Q$ values are slightly smaller than experiment. Moreover, fitting of the summed spectrum (see SI) gives $C_Q$ = 31 MHz, $\eta_Q$ = 0.05 and $C_Q$ = 31 MHz, $\eta_Q$ = 0.3 for the two types of $S_2^{2-}$ sites, in good agreement with the respective DFT-calculated values.

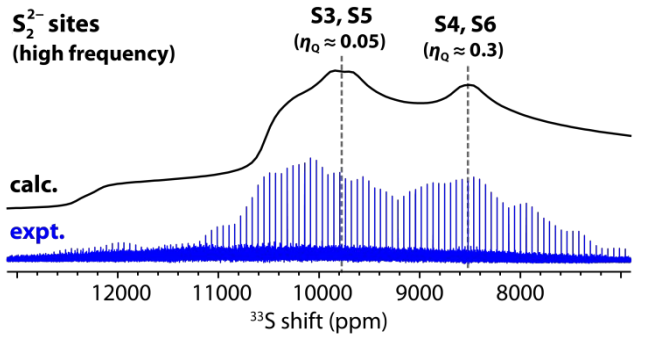


Figure 4: Focusing on the high-frequency region of the discontinuity arising from $S_2^{2-}$ sites, the simulated $^{33}S$ spectrum using DFT-calculated parameters ("calc.") and the experimental DFS-QCPMG VOCS static $^{33}S$ spectrum of $NbS_3$ acquired at 20 T in ~30 h ("expt."). The decrease in both signal and noise at the edges of the experimental data is due to the effective excitation bandwidth (5 subspectra were acquired, with carrier frequencies varying between ~8000 and ~12000 ppm and a constant step size of ~1000 ppm). Maxima arising from the two types of $S_2^{2-}$ sites are indicated with dashed grey lines. Full details are given in Table SI1 and the SI.

Although many of the spectra presented in this work necessitated long acquisition times of hours or days, it was possible to obtain evidence of the $S_2^{2-}$ sites in as short as 20 minutes with the carrier frequency on resonance with the high-frequency SOQ discontinuity (Figure SI9). This result gives us confidence that in future $^{33}S$ solid-state NMR will enable studies of redox mechanisms in cycled battery materials, by probing the disappearance and reappearance of these spectral signatures. $^{33}S$ enrichment of samples could also be used to significantly improve signal-to-noise levels.

In conclusion, we report natural-abundance $^{33}S$ solid-state NMR spectra of $NbS_3$, revealing the first spectral signatures of disulfide ($S_2^{2-}$) units, with the second-largest $^{33}S$ quadrupole

coupling constant (~31 MHz) measured to date. DFT calculations predict a characteristic splitting of the S sites due to the Peierls distortion in $NbS_3$, which is borne out by experiment. Future experiments on smaller quantities of $^{33}S$-enriched samples, subjected to electrochemical cycling, are deemed to be feasible in order to provide local insights into the anionic redox behaviour.

We are grateful to Dr Jeongjae Lee (University of Cambridge, UCAM) for advice regarding QCPMG, and to Dr Siân Dutton (UCAM) for assistance with synthesis. Dr Dinu Iuga (Facility Manager, UK 850 MHz Solid-state NMR Facility, University of Warwick) is also acknowledged. D.M.H. and S.B. acknowledge NECCES, an Energy Frontier Research Center funded by the U.S. Department of Energy, Office of Science, Basic Energy Sciences under Award No. DE-SC0012583. K.J.G. acknowledges a Herchel Smith scholarship (UCAM) and the EPSRC (EP/M009521/1). E.J. acknowledges the Swedish Research Council for funding. The periodic DFT calculations were performed using the UCAM HPC Service (http://www.hpc.cam.ac.uk/). The UK 850 MHz Solid-state NMR Facility was funded by EPSRC and BBSRC (no. PR140003), and the University of Warwick including part funding through Birmingham Science City Advanced Materials Projects 1 and 2 supported by Advantage West Midlands and the European Regional Development Fund.

## Notes and references

1 S. Britto, M. Leskes, X. Hua, C.-A. Hébert, H. S. Shin, S. Clarke, O. Borkiewicz, K. W. Chapman, R. Seshadri, J. Cho and C. P. Grey, *J. Am. Chem. Soc.*, 2015, **137**, 8499–8508.
2 N. Kumagai, K. Tanno and N. Kumagai, *Electrochim. Acta*, 1982, **27**, 1087–1092.
3 T. Yamamoto, S. Kikkawa and M. Koizumi, *J. Electrochem. Soc.*, 1986, **133**, 1558–1561.
4 W. Yuan and J. R. Günter, *Solid State Ionics*, 1995, **76**, 253–258.
5 D.-H. Seo, J. Lee, A. Urban, R. Malik, S. Kang and G. Ceder, *Nat. Chem.*, 2016, **8**, 692–697.
6 A. Débart, L. Dupont, R. Patrice and J.-M. Tarascon, *Solid State Sci.*, 2006, **8**, 640–651.
7 D. Golodnitsky and E. Peled, *Electrochim. Acta*, 1999, **45**, 335–350.
8 S. S. Zhang and D. T. Tran, *Electrochim. Acta*, 2015, **176**, 784–789.
9 F. Blanc, M. Leskes and C. P. Grey, *Acc. Chem. Res.*, 2013, **46**, 1952–1963.
10 O. Pecher, J. Carretero-González, K. J. Griffith and C. P. Grey, *Chem. Mater.*, 2017, **29**, 213–242.
11 A. Sutrisno, V. V. Terskikh and Y. Huang, *Chem. Commun.*, 2009, 186–188.
12 P. S. Belton, I. J. Cox and R. K. Harris, *J. Chem. Soc., Faraday Trans. 2*, 1985, **81**, 63–75.
13 W. A. Daunch and P. L. Rinaldi, *J. Magn. Reson., Ser. A*, 1996, **123**, 219–221.
14 H. J. Jakobsen, A. R. Hove, H. Bildsøe, J. Skibsted and M. Brorson, *Chem. Commun.*, 2007, **0**, 1629–1631.
15 A. Sasaki, L. Baquerizo Ibarra and S. Wimperis, *Phys. Chem. Chem. Phys.*, 2017, **19**, 24082–24089.
16 L. A. Huff, J. L. Rapp, J. A. Baughman, P. L. Rinaldi and A. A. Gewirth, *Surf. Sci.*, 2015, **631**, 295–300.
17 Y. Nakayama, R. Matsumoto, K. Kumagae, D. Mori, Y. Mizuno, S. Hosoi, K. Kamiguchi, N. Koshitani, Y. Inaba, Y. Kudo, H. Kawasaki, E. C. Miller, J. N. Weker and M. F. Toney, *Chem. Mater.*, 2018, **30**, 6318–6324.
18 L. A. O'Dell and I. L. Moudrakovski, *J. Magn. Reson.*, 2010, **207**, 345–347.
19 T. A. Wagler, W. A. Daunch, P. L. Rinaldi and A. R. Palmer, *J. Magn. Reson.*, 2003, **161**, 191–197.
20 T. A. Wagler, W. A. Daunch, M. Panzner, W. J. Youngs and P. L. Rinaldi, *J. Magn. Reson.*, 2004, **170**, 336–344.
21 P. J. Pallister, I. L. Moudrakovski, G. D. Enright and J. A. Ripmeester, *CrystEngComm*, 2013, **15**, 8808–8822.
22 R. W. Schurko, I. Hung and C. M. Widdifield, *Chem. Phys. Lett.*, 2003, **379**, 1–10.
23 M. R. Hansen, M. Brorson, H. Bildsøe, J. Skibsted and H. J. Jakobsen, *J. Magn. Reson.*, 2008, **190**, 316–326.
24 L. A. O'Dell, K. Klimm, J. C. C. Freitas, S. C. Kohn and M. E. Smith, *Appl. Magn. Reson.*, 2009, **35**, 247–259.
25 J. Rijnsdorp and F. Jellinek, *J. Solid State Chem.*, 1978, **25**, 325–328.
26 V. E. Fedorov, S. B. Artemkina, E. D. Grayfer, N. G. Naumov, Y. V. Mironov, A. I. Bulavchenko, V. I. Zaikovskii, I. V. Antonova, A. I. Komonov and M. V. Medvedev, *J. Mater. Chem. C*, 2014, **2**, 5479–5486.
27 T. Cornelissens, G. Van Tendeloo, J. Van Landuyt and S. Amelinckx, *Phys. Status Solidi A*, 1978, **48**, K5–K9.
28 M. A. Bloodgood, P. Wei, E. Aytan, K. N. Bozhilov, A. A. Balandin and T. T. Salguero, *APL Mater.*, 2018, **6**, 026602.
29 L. Houben, A. N. Enyashin, Y. Feldman, R. Rosentsveig, D. G. Stroppa and M. Bar-Sadan, *J. Phys. Chem. C*, 2012, **116**, 24350–24357.
30 J. B. Goodenough, *J. Solid State Chem.*, 1971, **3**, 490–500.
31 D. Paquet and P. Leroux-Hugon, *Phys. Rev. B*, 1980, **22**, 5284–5301.
32 A. Meerschaut, P. Grenouilleau, R. Brec, M. Evain and J. Rouxel, *J. Less Common Met.*, 1986, **116**, 229–250.
33 M. N. Kozlova, A. N. Enyashin and V. E. Fedorov, *J. Struct. Chem.*, 2016, **57**, 1505–1512.
34 S. J. Clark, M. D. Segall, C. J. Pickard, P. J. Hasnip, M. I. J. Probert, K. Refson and M. C. Payne, *Z. Kristallogr. - Cryst. Mater.*, 2005, **220**, 567–570.
35 J. V. Hanna, K. J. Pike, T. Charpentier, T. F. Kemp, M. E. Smith, B. E. G. Lucier, R. W. Schurko and L. S. Cahill, *Chem. Eur. J.*, 2010, **16**, 3222–3239.
36 F. A. Perras, C. M. Widdifield and D. L. Bryce, *Solid State Nucl. Magn. Reson.*, 2012, **45–46**, 36–44.
37 Y. Y. Tong, *J. Magn. Reson., Ser. A*, 1996, **119**, 22–28.
38 D. Massiot, I. Farnan, N. Gautier, D. Trumeau, A. Trokiner and J. P. Coutures, *Solid State Nucl. Magn. Reson.*, 1995, **4**, 241–248.
39 O. Pecher, D. M. Halat, J. Lee, Z. Liu, K. J. Griffith, M. Braun and C. P. Grey, *J. Magn. Reson.*, 2017, **275**, 127–136.
40 J. Autschbach, S. Zheng and R. W. Schurko, *Concepts Magn. Reson.*, 2010, **36A**, 84–126.
41 S. Sturniolo, T. F. G. Green, R. M. Hanson, M. Zilka, K. Refson, P. Hodgkinson, S. P. Brown and J. R. Yates, *Solid State Nucl. Magn. Reson.*, 2016, **78**, 64–70.

Table of Contents entry

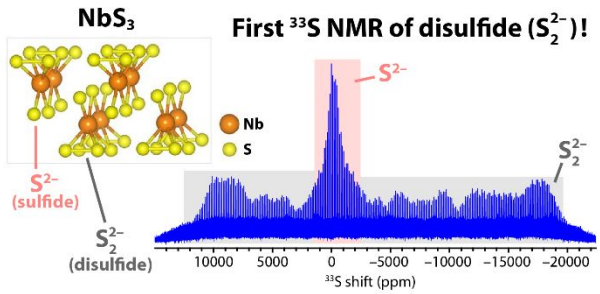


The first known solid-state $^{33}S$ NMR spectrum of disulfide ($S_2^{2-}$) anions is reported, in the Li-ion battery conversion material $NbS_3$.